Check for updates

ADVANCED QUANTUM TECHNOLOGIES
www.advquantumtech.com

High-Purity Single-Photon Emission in the Telecom O-Band from Droplet-Epitaxy InAs Quantum Dots Integrated into a GaAs/AlGaAs Planar Microcavity on Vicinal GaAs(111)A Platform

*Paweł Wyborski, Artur Tuktamyshev, Martin A. Jacobsen, Abdulmalik A. Madigawa, Stefano Vichi, Niels Gregersen, Stefano Sanguinetti, and Battulga Munkhbat**

Efficient single-photon emitters operating at telecom wavelengths are pivotal for implementing long-distance quantum communication through existing fiber-optic networks. Here, the realization of single-photon emission is reported in the second telecom window from droplet-epitaxy InAs quantum dots (QDs) integrated into a GaAs-based photonic structure. By employing an InAlAs metamorphic buffer layer to engineer strain, telecom-wavelength emission is achieved over a broad range of 1170–1360 nm, while maintaining compatibility with mature GaAs device platforms. Embedded in a planar GaAs/AlGaAs distributed Bragg reflector microcavity, these QDs exhibit high-purity single-photon emission, as indicated by a second-order correlation function $g^{(2)}(0) = 0.012^{+0.051}_{-0.012}$ under continuous-wave excitation and $g^{(2)}(0) = 0.069 \pm 0.032$ under pulsed above-band excitation. Time-resolved photoluminescence measurements yield a short average lifetime of about 0.98 ns, and the cavity design improves the extraction efficiency up to 5.8-fold, with a value of approximately 3.9% to the first lens. These results highlight the potential of droplet-epitaxy InAs QDs for scalable, fiber-compatible quantum photonic technologies and pave the way for practical long-distance quantum communication.

1. Introduction

Realizing secure, large-scale quantum communication and distributed quantum computing relies on the development of extended and reliable quantum networks.[1] At the heart of these networks lie quantum interconnects, enabling the coherent transfer of quantum states between distant nodes and thus facilitating entanglement distribution and state teleportation. Single photons are ideally suited as "flying qubits" in such architectures due to their robustness against decoherence and compatibility with optical fiber networks.[2] For practical implementations of quantum communication protocols, efficient single-photon sources operating within the telecommunication O-band (≈1310 nm) and C-band (≈1550 nm) are highly desirable.[3] These wavelength bands experience minimal loss in standard silica fibers, supporting long-distance photon transmission with lower attenuation. Additionally, exploiting the extensive infrastructure of classical telecommunication components, such as broadband modulators[4] and high-speed detectors,[5,6] further enhances the feasibility and scalability of quantum communication systems. Consequently, the development of single-photon emitters that combine high purity, brightness, and compatibility with telecom wavelengths is essential for future photonic quantum information technology.

The semiconductor quantum dot (QD) has recently emerged as a leading platform for on-demand single-photon and entangled-photon pair generation.[7,8] Engineered QDs have demonstrated record performance in terms of photon purity, indistinguishability, and brightness, particularly in the sub-1100 nm range. By integrating QDs into advanced photonic structures and employing electrical control, researchers have achieved near-ideal single-photon performance on GaAs platforms.[7,9] Extending these remarkable properties into the telecom band, however, requires careful epitaxial growth and strain engineering. Two main material systems have been explored for telecom-wavelength QDs: InAs/GaAs [10–12] and InAs/InP.[13–15] Among

P. Wyborski, M. A. Jacobsen, A. A. Madigawa, N. Gregersen, B. Munkhbat
Department of Electrical and Photonics Engineering
Technical University of Denmark
Kongens Lyngby 2800, Denmark
E-mail: bamunk@dtu.dk

A. Tuktamyshev, S. Vichi, S. Sanguinetti
L-NESS and Department of Materials Science
University of Milano-Bicocca
Milano 20216, Italy

The ORCID identification number(s) for the author(s) of this article can be found under https://doi.org/10.1002/qute.202500159

© 2025 The Author(s). Advanced Quantum Technologies published by Wiley-VCH GmbH. This is an open access article under the terms of the Creative Commons Attribution License, which permits use, distribution and reproduction in any medium, provided the original work is properly cited.

DOI: 10.1002/qute.202500159

these, GaAs-based platforms offer the advantage of straightforward integration with high-quality distributed Bragg reflectors (DBRs), facilitating the fabrication of planar microcavities and other advanced photonic architectures. Achieving telecom emission from InAs/GaAs QDs can be done with careful strain engineering by using metamorphic buffer layers (MMBLs) to relax the lattice mismatch, thus reducing strain-induced gap widening in InAs and shifting the emission into the O- and C-band ranges.[10,11,16–18] However, common InGaAs MMBL thickness on GaAs(001) exceeds 1 μm,[19,20] limiting their compatibility with photonic structures. The minimal thickness of the InGaAs MMBL on GaAs(001) reported in the literature is 180 nm with a total InGaAs layer thickness of about 450 nm.[17] A promising approach to minimize InGa(Al)As MMBL thickness on GaAs platform and to fabricate a telecom QD-based single-photon source integrated with the photonic cavity is to epitaxially grow on the (111)-oriented substrates. Due to rapid relaxation of compressive strain via the nucleation of the misfit dislocations net,[21–24] it is possible to grow thin ($\approx$ 30–40 nm) and flat metamorphic layers on the on-axis and vicinal GaAs(111)A.[24–26] Originally, (111)-oriented substrates are used to self-assemble highly-symmetrical QDs for the fine structure splitting (FSS) reduction that complicates the generation of polarization-entangled photon pairs.[27–30]

The formation of QDs on GaAs(111)A via the Stranski–Krastanov (SK) growth mode is not straightforward. SK growth mode, employed for the self-assembly of InAs/GaAs(001) QDs,[31] is not able to induce the self-assembly of 3D islands on GaAs(111)A surfaces because of the rapid relaxation of compressive strain via the insertion of misfit dislocations at the substrate-epilayer interface.[21–24] Due to growth defects, supersize islands can be obtained at high InAs coverages on GaAs(111)B.[32] Because of their defective nature and large size, such islands cannot act as QDs. Therefore, InAs/GaAs(111)A or InAs/InAl(Ga)As QDs can be obtained only by the droplet epitaxy method. Only by switching the strain from compressive to tensile in the epilayers, self-assembled GaAs QDs on InAl(Ga)As(111)A were demonstrated,[33,34] with a still limited control capability.

Droplet epitaxy enables control over QD size, shape, and density,[9,35] making it suited for achieving telecom-wavelength emission. While single-photon emitters based on droplet epitaxy QDs have been reported by several groups[14,36–42] using a range of semiconductor heterostructure combinations on (001) oriented substrates, the complete characterization of a quantum emitter in the telecom range using quantum dots grown on (111) substrates, to take profit of the reduced thickness for the complete relaxation of a metamorphic barrier, is still lacking.

The single photon emission at telecom wavelength from InAs/InGaAlAs QDs grown on InP(111)A substrates by droplet epitaxy was demonstrated with the second-order correlation function at zero delay $g^{(2)}(0)$ around 0.2 under continuous-wave (CW) excitation.[43] To increase extraction efficiency, a vertical optical cavity approach with thick DBR layers could be implemented. However, it is practically challenging to realize it on the singular (111) substrates due to the extremely low growth rate and the appearance of surface defects which hinders a 2D growth mode.[44–46] One solution is to utilize vicinal GaAs{111} substrates, which support sufficiently thick GaAs/AlGaAs DBRs. Indeed, droplet-epitaxy InAs/GaAs(111)B QDs emitting near 930 nm and integrated into a hybrid cavity–comprising a bottom GaAs/AlGaAs DBR and a microlens–have exhibited $g^{(2)}(0)$ = 0.07.[47,48] At telecom wavelengths, however, such fully integrated microcavity designs remain scarce. To the best of our knowledge, only one study has reported telecom droplet-epitaxy InAs QDs on GaAs(111)A into a GaAs-based microcavity via the insertion of an InGa(Al)As metamorphic layer, showing bright QDs with low FSS.[49] Despite these advances, single-photon characteristics and carrier dynamics of telecom droplet-epitaxy InAs/InAlAs(111)A QDs within GaAs-based microcavities – crucial for quantum network applications – have not yet been thoroughly investigated. Additionally, the study of the strain relaxation behavior of droplet epitaxy InAs/InAlAs(111)A QDs shows that the majority of QDs in refs. [49, 50] are optically inactive due to their large size.[51]

In this work, we present the characterization of a promising telecom single-photon source based on low-density InAs QDs embedded in a planar GaAs/AlGaAs distributed Bragg reflector microcavity. Telecom O-band emission from droplet-epitaxy InAs QDs grown on a GaAs(111)A substrate are achieved through precise strain engineering of the QDs using a uniform InAlAs metamorphic buffer layer and optimized QD growth parameters. QD size and shape improvements have been implemented, increasing the number of optically active QDs by decreasing the amount of indium deposited during the droplet nucleation step, subsequently decreasing the droplet and QD sizes and fabricating in-plane symmetric hexagonal-shaped QDs.[51] The QDs embedded within the planar $\lambda/2$ DBR microcavity demonstrate highly efficient single-photon emission with excellent purity. Measurements of the second-order correlation function reveal $g^{(2)}(0) = 0.012^{+0.051}_{-0.012}$ under continuous-wave (CW) excitation and $g^{(2)}(0) = 0.069 \pm 0.032$ under pulsed above-band excitation. Furthermore, time-resolved and power-dependent photoluminescence studies indicate a short average lifetime of approximately 0.98 ns and extraction efficiency around 3.9% to the first lens. These results highlight the potential of droplet-epitaxy InAs QDs integrated into GaAs-based photonic structures as a robust platform for single-photon generation at telecom wavelengths. It offers a promising platform for scalable quantum photonic technologies and opens new avenues for long-distance quantum communication.

2. Quantum Dot Sample

The QD sample used in this work was grown via molecular beam epitaxy (MBE) and features low-density InAs/InAlAs QDs on GaAs(111)A substrates with 2° miscut. The combination of the InAlAs metamorphic buffer layer and the droplet epitaxy method enabled the formation of QDs emitting in the telecom range on a GaAs-based substrate. This advancement opens possibilities for integrating telecom InAs QDs into GaAs-based photonic structures, benefiting from the extensive technological maturity and versatility of the GaAs platform. To exploit this advantage, we integrated the QDs into a planar microcavity to enhance the extraction efficiency of the single-photon source emission. The cavity is defined by a bottom-distributed Bragg reflector (DBR) consisting of 25 GaAs/AlGaAs pairs situated beneath the InAlAs layer, which contains the QDs and the buffer layer. The cavity is then completed with three GaAs/AlGaAs/GaAs layers on top of the InAlAs layer. We chose DBR layer thicknesses of $\lambda_{\text{eff}}/4$ and an

© 2025 The Author(s). Advanced Quantum Technologies published by Wiley-VCH GmbH

25119044, 0, Downloaded from https://advanced.onlinelibrary.wiley.com/doi/10.1002/qute.202500159 by POLITECNICO DI MILANO, Wiley Online Library on [26/06/2025]. See the Terms and Conditions (https://onlinelibrary.wiley.com/terms-and-conditions) on Wiley Online Library for rules of use; OA articles are governed by the applicable Creative Commons License

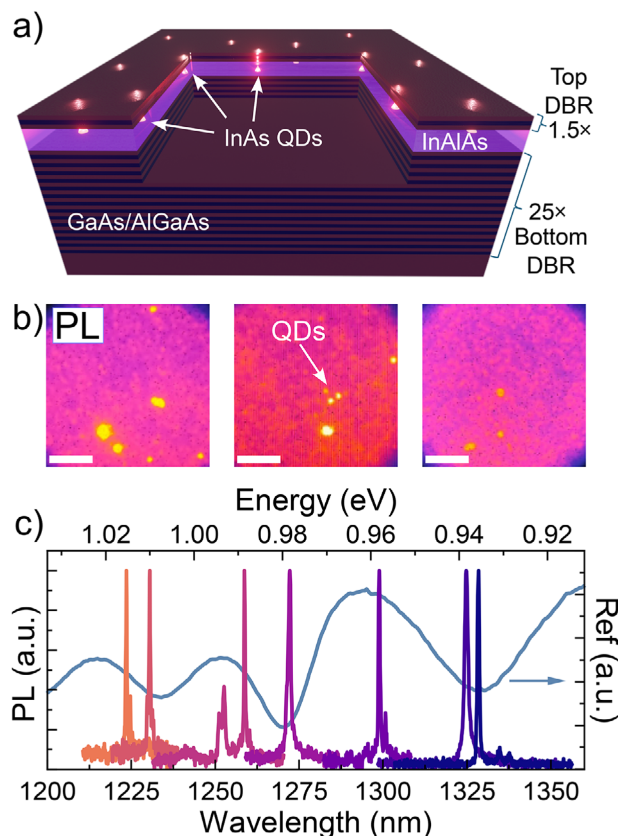

Figure 1. a) Schematic layout of sample presenting InAs QDs in InAlAs metamorphic buffer layer embedded into a photonic cavity, consists of a bottom and top DBRs. b) Low-temperature PL images of QDs emission recorded by the infrared camera after 660 nm LED excitation (the scale bare is 20 μm). c) PL spectra of exemplary single QDs and reflectivity spectrum of the planar microcavity (blue) ($T \approx 4$ K).

InAlAs thickness of $\lambda_{eff}/2$, where λ_{eff} is the effective wavelength in the material, to target a cavity resonance of around $\lambda \sim 1300$ nm. Reflectivity measurements, combined with a fitting procedure, will later confirm that the fabricated device's resonance is around $\lambda \sim 1330$ nm. The layout and schematic of the device are shown in **Figure 1a** and Figure S1 (Supporting Information). The top DBR structure, composed of standard GaAs-AlGaAs pairs, appears suboptimal due to the additional tensile strain between the metamorphic buffer layer and the DBR structure, resulting in a rough surface (root-mean square roughness = 20 nm on 5×5 μm^2 scan area; see Figure S2, Supporting Information). Such a high surface roughness likely increases scattering losses and degrades overall cavity performance. On a (111)-oriented substrate, compressive strain in InAlAs grown on GaAs is relaxed via the formation of misfit dislocations net[21,22] resulting in a flat surface.[25,26] Conversely, tensile strain in GaAs on InAlAs drives the formation of three-dimensional islands, whose size grow with increasing capping layer thickness.[33,44] However, the DBR structure cannot contain InGaAs layers lattice-matched to our InAlAs metamorphic buffer layer (60% indium) due to photon absorption at the telecom range. In the future, we plan to investigate the InAlAs-InGaAlAs layers, lattice-matched to the metamorphic buffer layer, as the top DBR pair.

The droplet epitaxy technique enables optimization of the shape and size of QDs by carefully adjusting fabrication parameters,[52] which is critical for achieving emission within the telecom range. In this work, we decreased the amount of deposited indium during the droplet nucleation step in contrast to QDs obtained in refs. [49, 50] in order to shift the center of QD height distribution below 3 nm to achieve a higher density of optically active QDs. QDs exceeding 2.5–3 nm height are plastically relaxed, resulting in the mass transfer onto QDs during capping layer deposition. Such dislocated QDs act as the non-radiative recombination centers.[51] Moreover, small droplet size and high As flux during the crystallization step lead to the fabrication of symmetrical hexagonal-shaped QDs as in the case of GaAs/AlGaAs(111)A QDs (see Figure S4, Supporting Information).[52] Detailed information about the fabrication process and corresponding structure analysis are provided in the Experimental Section as well as in Note S1 and Figures S2–S4 (Supporting Information). A broad distribution of QD sizes (see Figure S3a, Supporting Information) results in emissions ranging from 1100 to 1350 nm, with particular interest in the second telecom window. When the size of QDs increases, the emission wavelengths shift to longer wavelengths. Atomic force microscopy (AFM) analysis (Figures S3 and S4, Supporting Information) reveals symmetric QDs with increased height-to-diameter ratio for larger dots. Optimized growth parameters achieved a low QD surface density of approximately 1.5×10^8 cm^{-2}, as confirmed by AFM as well as by recorded photoluminescence (PL) images from the sample at 4K using an InGaAs CCD camera (Figure 1b). By applying a spectral bandpass filter centered at 1300 with a bandwidth of about 12 nm (FBH1300–12), only a few bright emission points were detected under the illumination of a 660 nm light-emitting diode (LED) as an excitation source, corresponding to individual QDs in the specified spectral range. However, the individual bright spots in the PL image do not provide complete optical properties and their single-photon characteristics.

3. Optical Characterization

3.1. Micro-photoluminescence Spectroscopy

To gain deeper insights into the optical properties of individual QDs, we performed micro-photoluminescence (μPL) spectroscopy from the sample at T $\approx$ 4 K. The sample was placed in a closed-cycle optical cryostat equipped with nanopositioners. The μPL spectra were acquired with an objective lens under the above-band excitation of $\lambda = 650$ nm laser excitation, passed through a single long-pass optical filter (LPF 1000 nm), and recorded with an optical spectrometer (Andor, InGaAs CCD camera). The measurement setup is described in more detail in the Experimental Section. Figure 1c shows the emission lines taken from several representative individual QDs, each exhibiting relatively narrow lines ranging from 1220 to 1330 nm. The broad spectral coverage provided by these individual QDs enables correlating their emission energies with various optical characteristics, including polarization anisotropy, photoluminescence decay time, and spectral broadening. These correlations, in turn, offer deeper insights into how the QD size distribution and the surrounding buffer layer influence their intrinsic properties, which will be discussed

 © 2025 The Author(s). Advanced Quantum Technologies published by Wiley-VCH GmbH

25119044, 0, Downloaded from https://advanced.onlinelibrary.wiley.com/doi/10.1002/qute.202500159 by POLITECNICO DI MILANO, Wiley Online Library on [26/06/2025]. See the Terms and Conditions (https://onlinelibrary.wiley.com/terms-and-conditions) on Wiley Online Library for rules of use; OA articles are governed by the applicable Creative Commons License

in the following sections. Additionally, to investigate to what extent the implemented resonant DBR microcavity enhances emission behavior, e.g., radiative decay rate and extraction efficiency, we measured the normal incidence reflectivity from the sample under a broad-band illumination. The obtained reflectivity spectrum shown in Figure 1c exhibits several broad peaks and dips. Fitting the full-range spectrum with the transfer-matrix formalism (see Note S2, Supporting Information) identifies the dip at 1330 nm as the cavity resonance. This resonance lies at the center of the high-reflectivity stopband, while all other peaks and dips arise from standard DBR features outside the stopband and do not correspond to resonant modes. The full range of the reflectivity spectrum and the corresponding transfer matrix fitting are plotted in Figure S5 (Supporting Information). The full width at half maximum (FWHM) of the cavity dip at 1330 nm is as broad as approximately 35 nm, which results in a low Q-factor of 38 as expected due to the leaky top DBR mirror (only 1.5 × GaAs/AlGaAs).

To examine how the resonant cavity and QD size influence the optical properties of individual QDs, we selected two representative QDs: one emitting at a shorter wavelength (1225 nm) and another at a longer wavelength (1325 nm), as shown in **Figure 2**. The choice of these two QDs serves two purposes. First, by comparing a QD with an emission resonant to the cavity to one whose emission lies outside the cavity resonance, we can isolate the cavity's impact on optical properties. Second, as the emission wavelength is closely related to QD size, comparing QDs at different wavelengths, combined with additional statistical data on QD size, allows us to more thoroughly investigate how size variations affect their intrinsic optical characteristics (Figure 2). Figure 2a–c present PL spectra, power-dependent PL intensity curves, and in-plane polarization-dependent PL signals for the two representative QDs (QD_A and QD_B) under the above-band optical excitation. The power-dependent PL measurements reveal clear exponents close to 1 based on power-law analysis for both QDs (Figure 2b), suggesting that observed emission likely originates from ground-state neutral excitons or charged exciton complexes.

Next, we examined the emission intensity as a function of detected polarization to determine the degree of linear polarization (DOLP). DOLP reflects the asymmetry in linear polarization of exciton complexes–both charged and neutral–which is influenced by the mixing of light- and heavy-hole states. In our case (Figure 2c), QD_A (emitting at 1225 nm) exhibits nearly zero DOLP, while QD_B (emitting near 1330 nm) shows a slightly more induced DOLP. Moreover, analysis of polarization anisotropy for a broad set of QDs shows an increase in DOLP value correlated with QD emission shift to longer wavelengths (see Figures S7, Supporting Information). This higher DOLP aligns with previous calculation results presenting the impact of the substrate miscut for QDs polarization anisotropy.[49] Moreover, our AFM measurements confirm that larger QDs possess a more significant aspect ratio between height and diameter (Figures S3, Supporting Information), possibly increasing the impact of miscut. The resulting conditions likely enhance the hole-state mixing for larger QDs, leading to increased DOLP values even for symmetrical QD (Figure S4, Supporting Information). The structural properties of the QDs, influenced mostly by substrate miscut and also growth dynamics, lead not only to measurable DOLP values but also reveal noticeable FSS, as discussed in previous studies.[49,50,53] The correlation between these two parameters is expected for QD based on the underlying structural and electronic properties of QDs,[54–56] but still, FSS and DOLP can not be strictly connected.[40,57] In this work, we also measured FSS values (see Figure S7 in Note S3, Supporting Information).

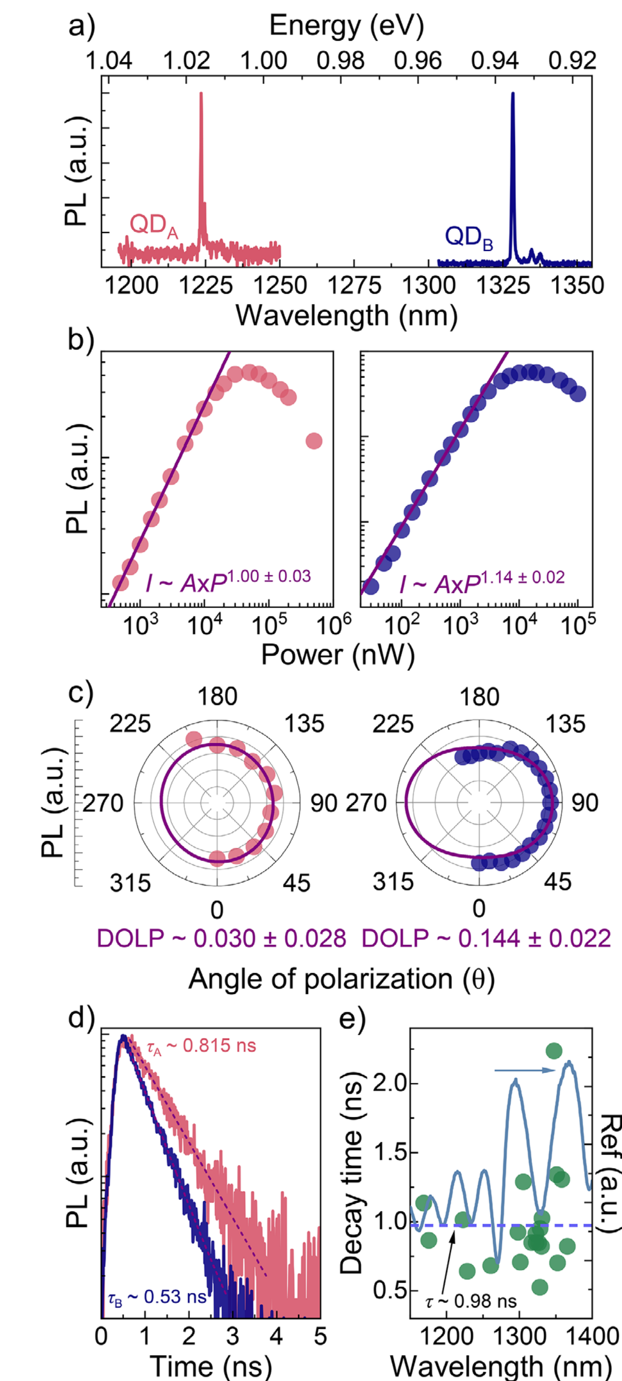

Figure 2. a) PL spectra of two exemplary QD_A (red) and QD_B (blue) emitting respectively out and in cavity spectral range. b) Power-dependent PL intensity plot, c) polarization-dependent PL intensity polar plot, and d) TRPL traces for QD_A and QD_B with respective fitting (purple). e) QDs decay time (green points) ranging from 1170 to 1350 nm, and the reflectivity spectrum (blue).

© 2025 The Author(s). Advanced Quantum Technologies published by Wiley-VCH GmbH

25119044, 0, Downloaded from https://advanced.onlinelibrary.wiley.com/doi/10.1002/qute.202500159 by POLITECNICO DI MILANO, Wiley Online Library on [26/06/2025]. See the Terms and Conditions (https://onlinelibrary.wiley.com/terms-and-conditions) on Wiley Online Library for rules of use; OA articles are governed by the applicable Creative Commons License

However, due to the finite resolution of our measurement system and the near-zero FSS values obtained, conclusively distinguishing between neutral and charged complexes remains beyond the scope of this study.

3.2. QDs Lifetime Characterization

For the identified single-QD emission lines from fundamental excitonic complexes, we measured the decay time using time-resolved photoluminescence (TRPL) at the lowest excitation powers, enabling the determination of the intrinsic QD lifetimes. Low-temperature and low-excitation-power conditions should limit the possible impact of non-radiative transitions and the dark exciton states dynamic or carrier escape to trap states and higher states. However, in our case, we cannot exclude these processes completely due to the observed increase in decay time in the function of excitation power (see Figure S8a in Note S4, Supporting Information). Figure 2d shows the measured TRPL histograms for QD_A and QD_B. From mono-exponential fittings, QD_B exhibits a shorter radiative lifetime of approximately 0.53 ns, while QD_A gives a slightly longer decay time of about 0.82 ns. Initially, this shorter lifetime for QD_B might suggest a possible Purcell enhancement due to better spectral alignment with the cavity resonance. To investigate this, we performed additional lifetime measurements on a broad set of QDs emitting between 1170 and 1360 nm (Figure 2e). The resulting data show a wide distribution of decay times, ranging from 0.5 ns to nearly 2 ns, with an average value of around 0.98 ns. Such variability indicates that the shorter decay time observed for QD_B is likely not a result of cavity-induced Purcell enhancement, but rather natural QD-to-QD variations. The exciton lifetimes measured here are in good agreement with those reported for telecom band QDs, which span from 0.18 to 3.2 ns with typical values around 1–2 ns.[11,40,57–63] The shortest lifetimes of 0.18 ns for MBE-grown SK InAs/InAlGaAs(001) QDs[58] and 0.34 ns for MOVPE droplet-epitaxy InAs/InGaAsP(001) QDs[59] were achieved from the QDs embedded in advanced photonic structures by combining Purcell enhancement and optimized excitation schemes.

Determining a clear relationship between decay time and emission wavelength is challenging. Although one might expect an inverse correlation–since larger QDs typically emit at longer wavelengths and might thus exhibit longer lifetimes–other factors complicate this picture. Emission energy depends not only on QD size, but also on indium composition and QD shape asymmetry, which can alter the oscillator strength (and QD lifetime) by modifying the wavefunctions of individual states. Without detailed theoretical calculations of excitonic states, directly comparing predicted and measured decay times remains difficult. Additionally, weak coupling with the cavity could influence decay times. However, comparing measured decay times with calculated Purcell factors as a function of wavelength (see Figure S8c, Supporting Information) does not support a strong cavity effect in these structures. Indeed, simulations confirm only a minimal Purcell factor (Fp) for these structures (see Note S4, Supporting Information). Despite this weak Purcell enhancement, the DBR microcavity still plays a crucial role in improving photon extraction efficiency – an effect we will discuss in the following sections.

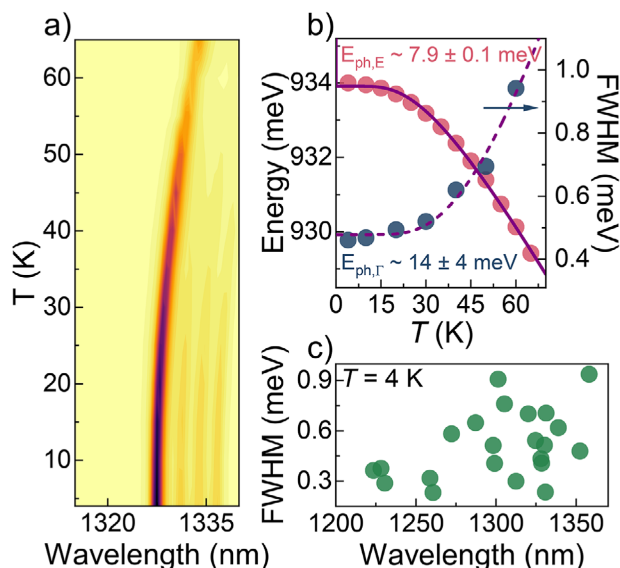

Figure 3. a) PL map for investigated line QD_B in the function of variable temperature. b) Energy emission (red points) and linewidth (blue points) for QD_B emission line (extracted by standard Gaussian profile fitting) in the function of temperature, together with respective fits (purple solid and dashed lines). c) Single QDs emission lines linewidth ranging from 1200 to 1350 nm.

3.3. Temperature Dependence

Before examining the cavity's effect on extraction efficiency, we first investigate the temperature-dependent optical properties of these QDs and characterize their single-photon emission properties. We confirmed that single-QD emission from these structures can be observed at temperatures as high as 65 K. Notably, the emission line identified at helium temperatures was still measurable at 65 K. **Figure 3a** presents photoluminescence map of the emission from a representative quantum dot from 4 to 65 K. The significant decrease in emission intensity at higher temperatures can be attributed to carriers escaping the QD due to increased thermal energy (see Note S5 and Figure S9, Supporting Information). In addition to reduced intensity, we also observed spectral broadening at elevated temperatures, likely induced by thermally activated phonons interacting with exciton. Moreover, the PL map in Figure 3a shows that the emission energy shifts with temperature, reflecting changes in the energy structure influenced by the crystal lattice and substrate temperature. By examining the temperature dependence of emission energy and linewidth (Figure 3b), we fit the observed variations to extract the energies of the phonons interacting with excitons. From the emission energy shift fit,[64] we obtained a phonon energy of 7.9 ± 0.1 meV. Similarly, the linewidth broadening fit[65,66] yielded an energy of 13.6 ± 3.4 meV. These values are comparable to known zone-edge transversal acoustic phonon energy in bulk GaAs and InAs (≈ 6 – 10 meV),[64] indicating a phonon-related influence on the emission line parameters. Deviations from the expected values in the case of linewidth dependence may arise from significant spectral diffusion, likely originating from the charge-trap-rich buffer layer. There are several sources of charged traps in the metamorphic InAlAs layer. First, the InAlAs/GaAs inter-

© 2025 The Author(s). Advanced Quantum Technologies published by Wiley-VCH GmbH

25119044, 0, Downloaded from https://advanced.onlinelibrary.wiley.com/doi/10.1002/qute.202500159 by POLITECNICO DI MILANO, Wiley Online Library on [26/06/2025]. See the Terms and Conditions (https://onlinelibrary.wiley.com/terms-and-conditions) on Wiley Online Library for rules of use; OA articles are governed by the applicable Creative Commons License

face contains a high density of misfit dislocations.[25] Second, we previously estimated a density of threading dislocations of around 1×10^{7} cm^{-2} in the InAlAs metamorphic layer.[50] Finally, to avoid step bunching resulting in a rough surface and evaporation of indium,[26] the InAlAs layer was grown at a relatively low temperature for an Al-containing layer, which can introduce point defects that act as carrier traps. Similar line broadening effects, caused by environmental charge fluctuations, have been reported in analogous structures containing buffer layers.[57,67–69] Moreover, observation of energy emission shift and linewidth modifications for QD emission lines in the function of the above-band excitation laser power (see Note S6 and Figure S10, Supporting Information) demonstrates the significant effect of the charge environment on the QD properties. Observed QD line broadening, which can exceed the Fourier-limited value, complicates the clear observation of phonon-induced broadening at lower temperatures. In our studied QDs, the measured broadening ranges from 230 to 940 μeV (Figure 3c), consistent with previous reports.[49,50] We found no clear correlation between the emission energy and the degree of broadening, indicating that variations in QD parameters affecting emission energy do not straightforwardly translate into changes in spectral linewidth.

3.4. Single-photon Purity

To confirm the single-photon emission character of these QDs, we performed second-order autocorrelation measurements under both CW and pulsed excitation conditions, as well as at elevated temperatures. **Figure 4** shows the second-order autocorrelation functions $g^{(2)}(\tau)$ for a QD emitting around 1330 nm. Under CW excitation, the $g^{(2)}(0)$ values are below 0.1 at both low (4 K) and elevated temperatures of 65 K (Figure 4a,b). Under pulsed excitation, $g^{(2)}(0)$ remains below 0.20 (Figure 4c). These values confirm single-photon emission behavior under the pulsed and CW excitation (more data presented in Note S7 and Figure S11, Supporting Information). Fitting the autocorrelation data yields slightly improved values of $0.012^{+0.051}_{-0.012}$ for CW excitation (4 K) and 0.069 ± 0.032 under pulsed excitation, after reducing noise contributions related to limited measurement counts. The values we obtain here are comparable with the high-purity single-photon emission reported for telecom-wavelength InAs/GaAs(001) and InAs/InP(001) QD systems,[11,60,70] particularly when using above-band excitation. Moreover, the non-zero $g^{(2)}(0)$ values with significant error values likely arise from background emission by other QDs within the detection spot and also a limited amount of coincidences, especially in the case of autocorrelation measurement for elevated temperatures. Under pulsed excitation, the need for higher excitation power to obtain sufficient coincidence counts can increase this background. Additionally, re-excitation processes may also contribute to the observed $g^{(2)}(0)$ values at higher excitation powers (see Figure S11, Supporting Information). The high defect density in the metamorphic buffer layer facilitates charge transfer between the quantum dot and nearby trap states, increasing the probability of such re-excitation events. To mitigate these issues, employing more selective excitation schemes, such as quasi-resonant or fully resonant excitation, could help isolate single QD emission. Furthermore, embedding the QDs within a p-i-n diode structure to stabilize the local charge environment can mitigate trap-related charge transfer and improve single-photon purity. Alternatively, spatially and spectrally selective resonant cavities could limit background emission by enhancing only specific QDs within the structure.

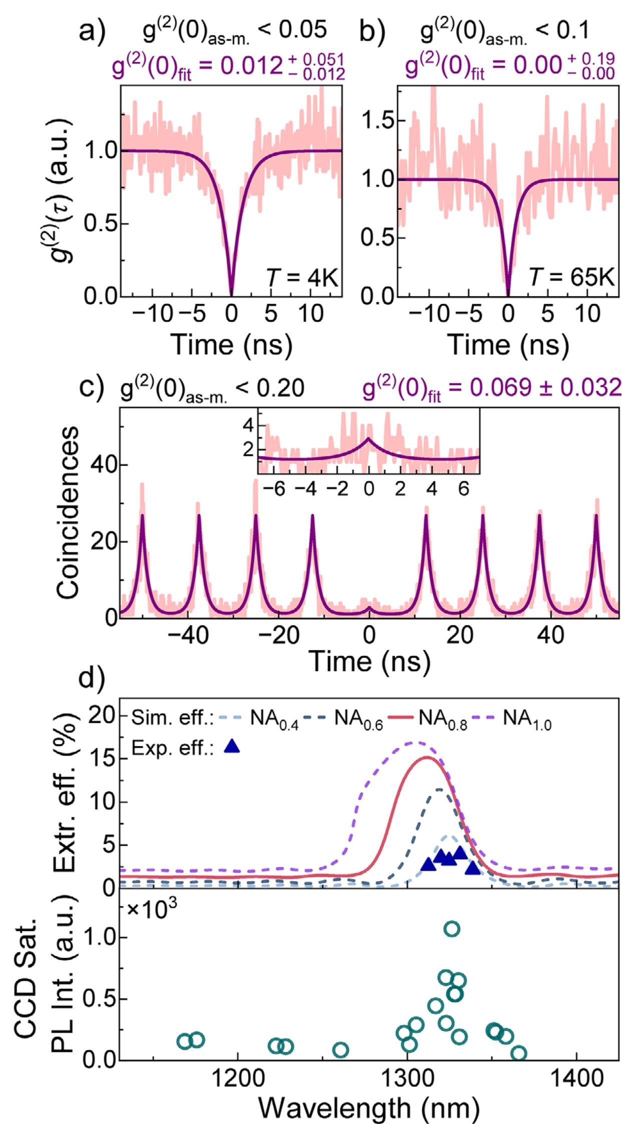

Figure 4. Second-order correlation function for QD emission under CW excitation in the case of a) low and b) elevated temperature. c) Autocorrelation coincidences plot for pulsed excitation. d) Comparison of a simulated extraction efficiency of emission value (lines in top panel) with saturation emission counts rate values on CCD under pulsed excitation for different QDs (green open points in bottom panel) in the function of emission wavelength. Additional points refer to experimentally determined extraction efficiency of QD emission values (blue triangle points in top panel).

3.5. Extraction Efficiency

To simulate the extraction efficiency (to the first lens) of our device, we have modeled the QD as a classical point dipole (for more

© 2025 The Author(s). Advanced Quantum Technologies published by Wiley-VCH GmbH

25119044, 0, Downloaded from https://advanced.onlinelibrary.wiley.com/doi/10.1002/qute.202500159 by POLITECNICO DI MILANO, Wiley Online Library on [26/06/2025]. See the Terms and Conditions (https://onlinelibrary.wiley.com/terms-and-conditions) on Wiley Online Library for rules of use; OA articles are governed by the applicable Creative Commons License

information, see Optical Simulation Section; Note S8, Supporting Information). We can then define the extraction efficiency as $\varepsilon(\mathrm{NA}) = P_{\mathrm{colleted}}(\mathrm{NA})/P_{\mathrm{T}}$, where P_{T} is the total emitted power, $P_{\mathrm{colleted}}(\mathrm{NA})$ is the total integrated power in the far field above the structure, and NA is the numerical aperture that defines the integration angle. In the top panel of Figure 4d, we present the simulated extraction efficiency as a function of the wavelength for various NAs of the collection lens. Despite the minimal Purcell enhancement, the extraction efficiency is increased around the cavity resonance $\lambda \sim 1330$ nm. At this wavelength, the bottom DBR has a stopband (for light emitted at normal incidence), which provides high reflection, $R \sim 0.8$, compared to the broadband reflection, $R \sim 0.35$, of the top DBR due to the air interface (see Figure S12 in Note S8, Supporting Information). Therefore, the emitted light will escape upwards, increasing the collection efficiency despite low Purcell enhancement. Outside the stopband, the top reflection is much stronger than the bottom, and thus, the emitted light will escape through the wafer, i.e., very low collection efficiency. However, a significant part of the light is emitted toward more horizontal angles, which can only be collected by a lens with large NA. This light, however, does not experience the stopband at $\lambda \sim 1330$ nm. As shown in Figure S13 in Note S8 (Supporting Information), the bottom DBR stopband blueshifts with increased angles therefore the peak collection efficiency also blueshifts when the NA is increased. Nonetheless, the simulation indicates that the extraction efficiency to the first lens can be increased in the spectral range ~1280–1340 nm, depending on the NA.

To experimentally verify this cavity-induced enhancement for the extraction efficiency, we measured the emission intensities of a handful number of individual QDs spanning a broad spectral range from 1160 to 1370 nm under pulsed excitation at experimentally obtained saturation level to ensure a fair comparison. As shown by the cyan points in the bottom panel of Figure 4d, QDs emitting around the cavity resonance exhibit up to a 5.8-fold increase in emission intensity compared to those emitting outside the cavity range. This observation qualitatively agrees with the predictions from our simulations, confirming that the implemented low-Q cavity provides an enhancement for extraction efficiency despite the weak Purcell effect. In practice, factors such as setup efficiency, the inability to fully capture emission from all complexes within a single QD, and limited accuracy of saturation levels characterization using above-band excitation introduce some uncertainties in determining the true extraction efficiency. Nonetheless, by carefully accounting for the optical setup efficiency (see Note S9, Supporting Information), we estimate a maximum extraction efficiency of about 3.9% (average value of 3.11 ±0.32%) to the first lens for QDs near the cavity resonance (see top panel Figure 4d; Table S1, Supporting Information). Obtained saturation emission counts rate for the best QDs exceed 40 kcps in the used setup configuration. Including setup efficiency-based correction, this value can be above 2 Mcps according to above 3% extraction efficiency. By improving setup efficiency value to around $10-20\%$,[12,71] QDs emission rate should show above 0.5 Mcps for investigated emitters embedded in the planar cavity without the application of more advanced and challenging deterministic photonic structures presenting much higher values of extraction efficiency.[12,15,72,73]

4. Discussion

The discrepancy between measured extraction efficiency values (about 3.9%) and the simulated results (up to 15%) likely arises from several factors related to both structural modeling and device performance. First, the simulation relied on a nominal structural design (see Figure S1, Supporting Information) that assumed the cavity would be centered at ~1280 nm (Figure S5, Supporting Information), in line with earlier findings.[49] In reality, local variations in layer thickness and composition shifted the actual cavity resonance to ~1330 nm. Although we fitted variable parameters such as layer composition and thickness, to match the measured reflectivity spectrum (Note S2, Supporting Information), uncertainties in refractive indices and the potential for less-probable fitting solutions complicate the accuracy of the final model. Moreover, the QDs themselves might not be precisely positioned within the $\lambda/2$ plane due to the double-step capping procedure, while strain, defects and roughness at the interfaces (particularly in the top DBR and buffer layer) can further alter the optical environment. The model used for the calculation can not include the sample imperfections driven by lattice constant differences in the InAlAs buffer layer and GaAs. In the top DBR, the strain from GaAs grown on InAlAs promotes 3D island formation, increasing surface roughness and exacerbating scattering losses that degrade photonic-structure performance. Further optimization of MBE growth parameters[26,46] as well as top DBR structure in the context of structure quality, together with precise control of QDs localization in cavity structure can still improve this possible limitation. Another potential source of the discrepancy is the assumption that the QDs have an internal quantum efficiency (IQE) of 1, considering the ideal case. However, in practice, non-radiative recombination pathways, particularly under above-band excitation, can diminish the effective photon generation rate.[63] Indeed, variations in decay rates at different excitation powers (see Figure S8, Supporting Information), suggest that some QDs may exhibit sub-unity IQE. Additionally, using high-power above-band excitation can complicate the process of fully saturating the exciton states, as it introduces significant background emission. To mitigate this issue, we lowered the excitation power, but this adjustment may result in an incomplete exciton population and thus contribute to the observed discrepancy between our measured extraction efficiency and simulated values. Moreover, injecting carriers in the charge-trap-rich buffer layer via high-energy above-band excitation may induce more spectral diffusion and broaden the QD emission lines. Such spectral broadening may exceed the monochromator's filtering bandwidth, reducing the fraction of collected photons. Optimizing the excitation schemes, preferably through resonant or quasi-resonant excitation, and implementing a p–i–n diode structure for electrical stabilization could achieve both full population inversion and more stable, high-brightness single-photon emission, ultimately enabling more accurate measurements of extraction efficiency.

Despite these discrepancies, the obtained values are still comparable to those reported in the telecom range for similar QDs with extraction efficiencies of $3-7\%$, achieved using bottom DBRs[74,75] or metallic mirror,[72] showing penitential of this platform in context of efficient single-photon sources fabrication. Further improvements are attainable through more

© 2025 The Author(s). Advanced Quantum Technologies published by Wiley-VCH GmbH

25119044, 0, Downloaded from https://advanced.onlinelibrary.wiley.com/doi/10.1002/qute.202500159 by POLITECNICO DI MILANO, Wiley Online Library on [26/06/2025]. See the Terms and Conditions (https://onlinelibrary.wiley.com/terms-and-conditions) on Wiley Online Library for rules of use; OA articles are governed by the applicable Creative Commons License

advanced photonic structures, such as horn,[76] circular Bragg grating,[12,15,58,77–80] mesa,[72,73,81–83] microlens,[84,85] photonic crystal,[86] tapered nanobeam cavity,[87] or open fiber cavity structure.[88] In addition to their inherently higher extraction efficiencies, alternative photonic elements, such as circular Bragg gratings, microlenses, and mesas, can overcome the performance limitations of the top DBR in our cavity, as they do not rely on a full DBR-based structure. Additionally, the implementation of such extra photonic structures (e.g., pillars, mesas) via the deterministic fabrication method[15,78,84,89–93] by exploiting the low-density feature of our QD sample can be employed to further boost the efficiency. Beyond extraction improvements, exploiting high-Q cavities can increase emission rates via Purcell enhancement,[12,15,58,78,86] especially if accompanied by fine spectral alignment of QDs to the cavity resonance via proper electrical tuning.[7] Moreover, such a high-Q photonic cavity combined with an implemented p-i-n structure is crucial to improve the important figure of merit - indistinguishability - for future applications of single-photon sources.[94] Especially here in the case of buffer-layer-based telecom QDs the reduction of electrical fluctuations (charge noise) affecting spectral diffusion[74,95] can be critically important to optimize this parameter. Besides optimizing the growth to minimize defects around the emitters, integrating the QDs into the aforementioned diode structure enables active electric-field control of local charges, thereby reducing spectral diffusion and charge-noise induced dephasing that limit coherence time and photon indistinguishability.[96,97] In addition to design optimizations, more sophisticated excitation schemes, such as p-shell,[12,15,58,77,78,82,87,98] LO-/LA-phonon,[15,59,99] two-photon,[74,96] resonant,[100] or SUPER-scheme[99] excitations can also be exploited to further develop these telecom QDs towards near-unity efficient single-photon sources with high indistinguishability.[7,15,74,94,96,98,99,101] Combined, these strategies could further elevate the performance of telecom QD single-photon sources for future photonic quantum information technologies.

5. Conclusion

In this work, we achieved single-photon emission in the telecom O-band from droplet-epitaxy InAs QDs grown on vicinal GaAs(111)A substrates using an optimized InAlAs metamorphic buffer layer. Integrating these QDs into a planar GaAs/AlGaAs DBR microcavity yielded high single-photon purity with $g^{(2)}(0)$ values of $0.012^{+0.051}_{-0.012}$ under CW and 0.069 ± 0.032 under pulsed excitations, and extraction efficiencies reaching 3.9% to the first lens near the cavity resonance. High-purity emission persists up to 65 K under CW excitation, with only limited Purcell enhancement but up to a 5.8-fold emission intensity improvement. Polarization-resolved measurements revealed increased DOLP for longer-wavelength QDs, linked to substrate miscut, while the overall optical quality (decay time and linewidth) remains robust across the 1200–1350 nm range. This suggests that shifting QD emission toward longer wavelengths does not compromise their intrinsic optical quality. These findings underscore the potential of droplet-epitaxy InAs QDs on GaAs(111)A for scalable, high-performance single-photon sources at telecom wavelengths.

6. Experimental Section

MBE Growth: The growth was carried out in a conventional MBE chamber equipped with effusion cells for Ga, Al, and In and the valved cracker cell for As. The sample was grown according to refs. [49–51] on a 2-inch undoped semi-insulating GaAs(111)A wafer with a miscut of 2° toward the $<\overline{1}\overline{1}2>$ direction. After loading the wafer into the growth chamber, the substrate temperature (T_s) was increased to 615 °C and kept for 10 min to clean the surface from the oxide layer. T_s was controlled by the *in-situ reflection high-energy electron diffraction (RHEED) technique and an appearance of (2*×2) surface reconstruction at 580 °C.[102] Then, the growth of a 100 nm–thick GaAs buffer layer and $Al_{0.5}Ga_{0.5}As$/GaAs distributed Bragg reflector (DBR) structure was performed at T_s of 600 °C with the growth rate of 0.5 and 1 ML/s for GaAs and AlGaAs layers, respectively (1 ML is the site-number density of the unreconstructed GaAs(001) surface defined as 6.26×10^{14} atoms/cm^2). During the growth of these layers, a beam equivalent pressure (BEP) of the As_4 flux was set about 3×10^{-5} torr measured by the ionization gauge. The DBR consists of 25 pairs with thicknesses of 102.5 and 96.1 nm for AlGaAs and GaAs, respectively, and it has high reflectivity (≈ 99%) for a wavelength range centered around 1310 nm. The $Al_{0.5}Ga_{0.5}As$/GaAs pair was chosen to avoid the oxidation of pure AlAs and decrease the DBR structure's growth time without growth interruptions for changing and stabilizing Ga and Al cell temperatures. After the growth of the DBR, T_s was set to 470 °C for the growth of a 100.8 nm–thick $In_{0.6}Al_{0.4}As$ metamorphic layer with the growth rate of 0.5 ML/s according to ref. [26] The As BEP during the growth of the InAlAs layer was about 1.5×10^{-5} torr. The QD self-assembly was performed using the droplet epitaxy procedure.[9,35] T_s was decreased to 370 °C and the As valve and shutter were closed to reach ultra-high vacuum conditions for the deposition of In. When the residual pressure in the chamber reached ≈ 3×10^{-9} torr, 0.15 ML of indium was deposited at the rate of 0.01 ML/s. The crystallization step was carried out at 300 °C by opening the As valve and shutter to expose the surface by the As flux for 3 minutes at the As BEP of 4.2×10^{-5} torr, followed by 5 minutes at the reduced As BEP of 1.5×10^{-5} torr. The capping $In_{0.6}Al_{0.4}As$ layer was grown at two stages. First 10 nm at T_s of 300 °C to avoid adatom diffusion out of InAs islands and then T_s was set to 470 °C without closing the fluxes. The InAlAs growth rate was 0.5 ML/s, and As BEP was 2.4×10^{-5} torr. Finally, the InAlAs cavity was covered by the GaAs/$Al_{0.5}Ga_{0.5}As$ 1.5–pair grown at the same conditions as the bottom DBR structure. The surface morphology of the different growth stages is present in Figure S2 (Supporting Information).

Morphological Analysis: The surface morphology was analyzed by the Veeco Innova AFM in tapping mode using Nanosensors SSS-NCHR sharp silicon tips capable of a lateral resolution of about 2 nm. The samples were mounted to have one of the cleavage edges $\langle\overline{1}\overline{1}2\rangle$ parallel to the x-scan direction. AFM scans have 512×512 or 1024×1024 pixel resolution. The scanning rate was set to 0.5 Hz.

Optical Characterization: The optical measurements were obtained with a custom-built low-temperature micro-photoluminescence (μ PL) setup. The sample is mounted on a closed-cycle cryostat (attoDRY800xs, Attocube) operating at a base temperature of 4 K with control of sample temperature to perform temperature-dependent studies. The cryostat is equipped with piezoelectric nanopositioners and a microscope objective (100×, NA = 0.7, long-working distance M Plan Apo NIR HR Mitutoyo objective or 60×, NA = 0.8, LT-APO/Telecom Attocube objective depending on used configuration with objective outside or inside the cryostat chamber). Excitation was performed with above-band excitation 650 nm semiconductor diode laser (LDH-D-C-650, PicoQuant) with CW and pulsed operation mode with below 90-ps-long pulses and a pulse-train control possibility (2.5–80 MHz). PL characterization was based on a 0.328 m focal-length monochromator (Kymera 328i, gratings: 150, 600 lines/mm, Andor, Oxford Instruments) with deep thermo-electrically-cooled InGaAs linear array detector (iDus, Andor, Oxford Instruments). The maximum resolution of the setup was obtained up to 0.09 meV. Time-correlated single-photon-counting mode was used to perform time-resolved PL characterization and single photon statistics measurements using Hanbury Brown and Twiss configuration (based on 50:50 fiber beam-splitter). As a detection setup, in that case, we used a single photon counting module

© 2025 The Author(s). Advanced Quantum Technologies published by Wiley-VCH GmbH

25119044, 0, Downloaded from https://advanced.onlinelibrary.wiley.com/doi/10.1002/qute.202500159 by POLITECNICO DI MILANO, Wiley Online Library on [26/06/2025]. See the Terms and Conditions (https://onlinelibrary.wiley.com/terms-and-conditions) on Wiley Online Library for rules of use; OA articles are governed by the applicable Creative Commons License

(Time Tagger Ultra, Swabian Instruments) together with superconducting nanowire single-photon detectors (ID281 SNSPD, ID Quantique). The polarization-resolved PL characterizations were obtained with the pair of half-wave plate and linear-polarizator. The setup efficiency characterization including transmission of all optical elements is present in Table S1 of the Note S9 (Supporting Information).

Optical Simulation: As mentioned, we model the QD as a classical point dipole with in-plane orientation and harmonic time dependence at frequency ω to calculate the extraction efficiency presented in Figure 4d. The corresponding current density is $\mathbf{J}(\mathbf{r}) = -i\omega\mathbf{p}\delta(\mathbf{r}-\mathbf{r}_d)$, where $\mathbf{r}_d$ is the position of the QD and $\mathbf{p}$ is the dipole moment. We then solve Maxwell's equation in the frequency domain by using an eigenmode method (similar to the Fourier modal method[103]) combined with a standard scattering matrix formalism.[104] Due to the simplicity of the planar cavity, both the eigenmodes and the scattering matrices can be found analytically. The method is described in further detail in Note S8 (Supporting Information).

Supporting Information

Supporting Information is available from the Wiley Online Library or from the author.

Acknowledgements

The authors acknowledge support from the European Research Council (ERC-StG "TuneTMD", grant no. 101076437) and the Villum Foundation (grant no. VIL53033). The authors also acknowledge the European Research Council (ERC-CoG "Unity", grant no. 865230), Carlsberg Foundation (grant no. CF21-0496), and the PNRR MUR project "National Quantum Science and Technology Institute" - NQSTI (PE0000023). Last but not least, the authors acknowledge the cleanroom facilities at DTU Nanolab – National Centre for Nano Fabrication and Characterization.

Conflict of Interest

The authors declare no conflict of interest.

Author Contributions

P.W. and A.T. contributed equally to this work. A.T. prepared the quantum dot samples and performed the morphological analysis of the grown quantum dots. M.J., and S.V. supported the project with theoretical calculations and valuable discussions. P.W. and A.M. performed full optical characterizations. P.W. performed data analysis and processing of all the optical data. N.G., S.S., and B.M. supervised and coordinated the project. P.W., A.T., N.G., S.S., and B.M. wrote the manuscript with the input of all coauthors.

Data Availability Statement

The data that support the findings of this study are available from the corresponding author upon reasonable request.

Keywords

droplet epitaxy, metamorphic buffer layer, high-purity single-photon emission, optical planar microcavity, single-photon source, telecom QDs, vicinal GaAs(111)A

Received: February 27, 2025
Revised: April 23, 2025
Published online:

[1] H. J. Kimble, *Nature* **2008**, *453*, 1023.
[2] D. A. Vajner, L. Rickert, T. Gao, K. Kaymazlar, T. Heindel, *Adv. Quantum Technol* **2022**, *5*, 2100116.
[3] (Ed.: P. Michler), *Quantum Dots for Quantum Information Technologies*, Nano-Optics and Nanophotonics, Springer, Cham **2017**.
[4] M. He, M. Xu, Y. Ren, J. Jian, Z. Ruan, Y. Xu, S. Gao, S. Sun, X. Wen, L. Zhou, L. Liu, C. Guo, H. Chen, S. Yu, L. Liu, X. Cai, *Nat. Photon.* **2019**, *13*, 359.
[5] J. Zhang, M. A. Itzler, H. Zbinden, J.-W. Pan, *Light Sci. Appl.* **2015**, *4*, e286.
[6] F. Marsili, V. B. Verma, J. A. Stern, S. Harrington, A. E. Lita, T. Gerrits, I. Vayshenker, B. Baek, M. D. Shaw, R. P. Mirin, S. W. Nam, *Nat. Photon.* **2013**, *7*, 210.
[7] P. Senellart, G. Solomon, A. White, *Nat. Nanotech.* **2017**, *12*, 1026.
[8] C. Couteau, S. Barz, T. Durt, T. Gerrits, J. Huwer, R. Prevedel, J. Rarity, A. Shields, G. Weihs, *Nat. Rev. Phys.* **2023**, *5*, 326.
[9] M. Gurioli, Z. Wang, A. Rastelli, T. Kuroda, S. Sanguinetti, *Nat. Mater.* **2019**, *18*, 799.
[10] E. S. Semenova, R. Hostein, G. Patriarche, O. Mauguin, L. Largeau, I. Robert-Philip, A. Beveratos, A. Lemaître, *J. Appl. Phys.* **2008**, *103*, 103533.
[11] S. L. Portalupi, M. Jetter, P. Michler, *Semicond. Sci. Technol.* **2019**, *34*, 053001.
[12] C. Nawrath, R. Joos, S. Kolatschek, S. Bauer, P. Pruy, F. Hornung, J. Fischer, J. Huang, P. Vijayan, R. Sittig, M. Jetter, S. L. Portalupi, P. Michler, *Adv. Quantum Technol.* **2023**, *6*, 2300111.
[13] X. Cao, M. Zopf, F. Ding, *J. Semicond.* **2019**, *40*, 071901.
[14] J. Skiba-Szymanska, R. M. Stevenson, C. Varnava, M. Felle, J. Huwer, T. Müller, A. J. Bennett, J. P. Lee, I. Farrer, A. B. Krysa, P. Spencer, L. E. Goff, D. A. Ritchie, J. Heffernan, A. J. Shields, *Phys. Rev. Appl.* **2017**, *8*, 014013.
[15] P. Holewa, D. A. Vajner, E. Zięba-Ostój, M. Wasiluk, B. Gaál, A. Sakanas, M. Burakowski, P. Mrowiński, B. Krajnik, M. Xiong, K. Yvind, N. Gregersen, A. Musiał, A. Huck, T. Heindel, M. Syperek, E. Semenova, *Nat. Commun.* **2024**, *6*, 2300111.
[16] L. Seravalli, P. Frigeri, G. Trevisi, S. Franchi, *Appl. Phys. Lett.* **2008**, *92*, 213104.
[17] R. Sittig, C. Nawrath, S. Kolatschek, S. Bauer, R. Schaber, J. Huang, P. Vijayan, P. Pruy, S. L. Portalupi, M. Jetter, P. Michler, *Nanophotonics* **2022**, *11*, 1109.
[18] B. Scaparra, E. Sirotti, A. Ajay, B. Jonas, B. Costa, H. Riedl, P. Avdienko, I. D. Sharp, G. Koblmüller, E. Zallo, J. J. Finley, K. Müller, *ACS Appl. Nano Mater.* **2024**, *7*, 26854.
[19] M. Paul, F. Olbrich, J. Höschele, S. Schreier, J. Kettler, S. L. Portalupi, M. Jetter, P. Michler, *Appl. Phys. Lett.* **2017**, *111*, 033102.
[20] K. D. Zeuner, K. D. Jöns, L. Schweickert, C. Reuterskiöld Hedlund, C. Nuñez Lobato, T. Lettner, K. Wang, S. Gyger, E. Schöll, S. Steinhauer, M. Hammar, V. Zwiller, *ACS Photonics* **2021**, *8*, 2337.
[21] H. Yamaguchi, J. G. Belk, X. M. Zhang, J. L. Sudijono, M. R. Fahy, T. S. Jones, D. W. Pashley, B. A. Joyce, *Phys. Rev. B* **1997**, *55*, 1337.
[22] A. Ohtake, M. Ozeki, *Phys. Rev. Lett.* **2000**, *84*, 4665.
[23] A. Ohtake, T. Mano, Y. Sakuma, *Sci. Rep.* **2020**, *10*, 4606.
[24] T. Mano, A. Ohtake, T. Kuroda, *Phys. Status Solidi A* **2024**, *221*, 2300767.
[25] T. Mano, K. Mitsuishi, N. Ha, A. Ohtake, A. Castellano, S. Sanguinetti, T. Noda, Y. Sakuma, T. Kuroda, K. Sakoda, *Cryst. Growth Des.* **2016**, *16*, 5412.
[26] A. Tuktamyshev, S. Vichi, F. Cesura, A. Fedorov, S. Bietti, D. Chrastina, S. Tsukamoto, S. Sanguinetti, *J. Cryst. Growth* **2022**, *600*, 126906.
[27] R. Singh, G. Bester, *Phys. Rev. Lett.* **2009**, *103*, 063601.
[28] M. Jo, T. Mano, M. Abbarchi, T. Kuroda, Y. Sakuma, K. Sakoda, *Cryst. Growth Des.* **2012**, *12*, 1411.

© 2025 The Author(s). Advanced Quantum Technologies published by Wiley-VCH GmbH

25119044, 0, Downloaded from https://advanced.onlinelibrary.wiley.com/doi/10.1002/qute.202500159 by POLITECNICO DI MILANO, Wiley Online Library on [26/06/2025]. See the Terms and Conditions (https://onlinelibrary.wiley.com/terms-and-conditions) on Wiley Online Library for rules of use; OA articles are governed by the applicable Creative Commons License

[29] T. Kuroda, T. Mano, N. Ha, H. Nakajima, H. Kumano, B. Urbaszek, M. Jo, M. Abbarchi, Y. Sakuma, K. Sakoda, I. Suemune, X. Marie, T. Amand, *Phys. Rev. B* **2013**, *88*, 041306(R).
[30] F. B. Basset, S. Bietti, M. Reindl, L. Esposito, A. Fedorov, D. Huber, A. Rastelli, E. Bonera, R. Trotta, S. Sanguinetti, *Nano Lett.* **2018**, *18*, 505.
[31] J. X. Chen, A. Markus, A. Fiore, U. Oesterle, R. P. Stanley, J. F. Carlin, R. Houdré, M. Ilegems, L. Lazzarini, L. Nasi, M. T. Todaro, E. Piscopiello, R. Cingolani, M. Catalano, J. Katcki, J. Ratajczak, *J. Appl. Phys.* **2002**, *91*, 6710.
[32] H. Wen, Z. M. Wang, J. L. Shultz, B. L. Liang, G. J. Salamo, *Phys. Rev. B* **2004**, *70*, 205307.
[33] C. D. Yerino, P. J. Simmonds, B. Liang, D. Jung, C. Schneider, S. Unsleber, M. Vo, D. L. Huffaker, S. Höfling, M. Kamp, M. L. Lee, *Appl. Phys. Lett.* **2014**, *105*, 251901.
[34] C. F. Schuck, S. K. Roy, T. Garrett, Q. Yuan, Y. Wang, C. I. Cabrera, K. A. Grossklaus, T. E. Vandervelde, B. Liang, P. J. Simmonds, *Sci. Rep.* **2019**, *9*, 18179.
[35] S. Sanguinetti, S. Bietti, N. Koguchi, *Droplet Epitaxy of Nanostructures*, Elsevier, **2018**, pp. 293–314.
[36] T. Müller, J. Skiba-Szymanska, A. B. Krysa, J. Huwer, M. Felle, M. Anderson, R. M. Stevenson, J. Heffernan, D. A. Ritchie, A. J. Shields, *Nat. Commun.* **2018**, *9*, 862.
[37] M. Anderson, T. Müller, J. Huwer, J. Skiba-Szymanska, A. B. Krysa, R. M. Stevenson, J. Heffernan, D. A. Ritchie, A. J. Shields, *npj Quantum Inf.* **2020**, *6*, 14.
[38] E. M. Sala, Y. I. Na, M. Godsland, A. Trapalis, J. Heffernan, *Phys. Status Solidi RRL* **2020**, *14*, 2000173.
[39] A. Chellu, J. Hilska, J.-P. Penttinen, T. Hakkarainen, *APL Mater.* **2021**, *9*, 051116.
[40] P. Holewa, S. Kadkhodazadeh, M. Gawełczyk, P. Baluta, A. Musiał, V. G. Dubrovskii, M. Syperek, E. Semenova, *Nanophotonics* **2022**, *11*, 1515.
[41] D. Deutsch, C. Buchholz, V. Zolatanosha, K. D. Jöns, D. Reuter, *AIP Adv.* **2023**, *13*, 055009.
[42] J. Michl, G. Peniakov, A. Pfenning, J. Hilska, A. Chellu, A. Bader, M. Guina, S. Höfling, T. Hakkarainen, T. Huber-Loyola, *Adv. Quantum Tech.* **2023**, *6*, 2300180.
[43] N. Ha, T. Mano, S. Dubos, T. Kuroda, Y. Sakuma, K. Sakoda, *Appl. Phys. Express* **2020**, *13*, 025002.
[44] L. Esposito, S. Bietti, A. Fedorov, R. Nötzel, S. Sanguinetti, *Phys. Rev. Mater.* **2017**, *1*, 024602.
[45] F. Herzog, M. Bichler, G. Koblmüller, S. Prabhu-Gaunkar, W. Zhou, M. Grayson, *Appl. Phys. Lett.* **2012**, *100*, 192106.
[46] A. Tuktamyshev, S. Vichi, S. Bietti, A. Fedorov, S. Sanguinetti, *Cryst. Growth Des.* **2024**, *24*, 9673.
[47] V. A. Gaisler, I. A. Derebezov, A. V. Gaisler, D. V. Dmitriev, A. I. Toropov, S. Fischbach, A. Schlehahn, A. Kaganskiy, T. Heindel, S. Bounouar, S. Rodt, S. Reitzenstein, *Optoelectron. Instrument. Proc.* **2017**, *53*, 178.
[48] I. A. Derebezov, V. A. Gaisler, A. V. Gaisler, D. V. Dmitriev, A. I. Toropov, M. von Helversen, C. de la Haye, S. Bounouar, S. Reitzenstein, *Semiconductors* **2019**, *53*, 1304.
[49] A. Barbiero, A. Tuktamyshev, G. Pirard, J. Huwer, T. Müller, R. Stevenson, S. Bietti, S. Vichi, A. Fedorov, G. Bester, S. Sanguinetti, A. Shields, *Phys. Rev. Applied* **2022**, *18*, 034081.
[50] A. Tuktamyshev, A. Fedorov, S. Bietti, S. Vichi, K. D. Zeuner, K. D. Jöns, D. Chrastina, S. Tsukamoto, V. Zwiller, M. Gurioli, S. Sanguinetti, *Appl. Phys. Lett.* **2021**, *118*, 133102.
[51] A. Tuktamyshev, S. Vichi, F. Cesura, A. Fedorov, G. Carminati, D. Lambardi, J. Pedrini, E. Vitiello, F. Pezzoli, S. Bietti, S. Sanguinetti, *Nanomaterials* **2022**, *12*, 3571.
[52] S. Bietti, F. B. Basset, A. Tuktamyshev, E. Bonera, A. Fedorov, S. Sanguinetti, *Sci. Rep.* **2020**, *10*, 6532.
[53] G. Pirard, F. Basso Basset, S. Bietti, S. Sanguinetti, R. Trotta, G. Bester, *Phys. Rev. B* **2023**, *107*, 205417.
[54] A. Musiał, P. Gold, J. Andrzejewski, A. Löffler, J. Misiewicz, S. Höfling, A. Forchel, M. Kamp, G. Sęk, S. Reitzenstein, *Phys. Rev. B* **2014**, *90*, 045430.
[55] E. Tsitsishvili, *Physica E* **2017**, *87*, 161.
[56] X. Yuan, S. F. Covre da Silva, D. Csontosová, H. Huang, C. Schimpf, M. Reindl, J. Lu, Z. Ni, A. Rastelli, P. Klenovský, *Phys. Rev. B* **2023**, *107*, 235412.
[57] P. Wyborski, M. Gawełczyk, P. Podemski, P. A. Wroński, M. Pawlyta, S. Gorantla, F. Jabeen, S. Höfling, G. Sęk, *Phys. Rev. Applied* **2023**, *20*, 044009.
[58] J. Kaupp, Y. Reum, F. Kohr, J. Michl, Q. Buchinger, A. Wolf, G. Peniakov, T. Huber-Loyola, A. Pfenning, S. Höfling, *Adv. Quantum Technol.* **2023**, *6*, 2300242.
[59] C. L. Phillips, A. J. Brash, M. Godsland, N. J. Martin, A. Foster, A. Tomlinson, R. Dost, N. Babazadeh, E. M. Sala, L. Wilson, J. Heffernan, M. S. Skolnick, A. M. Fox, *Sci. Rep.* **2024**, *14*.
[60] P. Holewa, D. A. Vajner, E. Zięba-Ostój, M. Wasiluk, B. Gaál, A. Sakanas, M. Burakowski, P. Mrowiński, B. Krajnik, M. Xiong, K. Yvind, N. Gregersen, A. Musiał, A. Huck, T. Heindel, M. Syperek, E. Semenova, *Nat. Commun.* **2024**, *15*, 3358.
[61] A. Musiał, P. Holewa, P. Wyborski, M. Syperek, A. Kors, J. P. Reithmaier, G. Sęk, M. Benyoucef, *Adv. Quantum Technol.* **2020**, *3*, 1900082.
[62] M. Anderson, T. Müller, J. Skiba-Szymanska, A. B. Krysa, J. Huwer, R. M. Stevenson, J. Heffernan, D. A. Ritchie, A. J. Shields, *Appl. Phys. Lett.* **2021**, *118*, 014003.
[63] J. Große, P. Mrowiński, N. Srocka, S. Reitzenstein, *Appl. Phys. Lett.* **2021**, *119*, 061103.
[64] D. G. Nahri, C. H. R. Ooi, *J. Opt. Soc. Am. B* **2014**, *31*, 1182.
[65] D. Gammon, E. S. Snow, B. V. Shanabrook, D. S. Katzer, D. Park, *Science* **1996**, *273*, 87.
[66] G. Moody, M. E. Siemens, A. D. Bristow, X. Dai, D. Karaiskaj, A. S. Bracker, D. Gammon, S. T. Cundiff, *Phys. Rev. B* **2011**, *83*, 115324.
[67] L. Seravalli, G. Trevisi, P. Frigeri, D. Rivas, G. Muñoz-Matutano, I. Suárez, B. Alén, J. Canet-Ferrer, J. P. Martínez-Pastor, *Appl. Phys. Lett.* **2011**, *98*, 173112.
[68] L. Seravalli, G. Trevisi, G. Muñoz-Matutano, D. Rivas, J. Martinez-Pastor, P. Frigeri, *Cryst. Res. Technol.* **2014**, *49*, 540.
[69] G. Muñoz-Matutano, D. Barrera, C. Fernández-Pousa, R. Chulia-Jordan, L. Seravalli, G. Trevisi, P. Frigeri, S. Sales, J. Martínez-Pastor, *Sci. Rep.* **2016**, *6*, 2045.
[70] Ł. Dusanowski, P. Holewa, A. Maryński, A. Musiał, T. Heuser, N. Srocka, D. Quandt, A. Strittmatter, S. Rodt, J. Misiewicz, S. Reitzenstein, G. Sęk, *Opt. Express* **2017**, *25*, 31122.
[71] A. Barbiero, J. Huwer, J. Skiba-Szymanska, D. J. P. Ellis, R. M. Stevenson, T. Müller, G. Shooter, L. E. Goff, D. A. Ritchie, A. J. Shields, *ACS Photonics* **2022**, *9*, 3060.
[72] P. Holewa, A. Sakanas, U. M. Gür, P. Mrowiński, A. Huck, B.-Y. Wang, A. Musiał, K. Yvind, N. Gregersen, M. Syperek, E. Semenova, *ACS Photonics* **2022**, *9*, 2273.
[73] A. Musiał, M. Mikulicz, P. Mrowiński, A. Zielińska, P. Sitarek, P. Wyborski, M. Kuniej, J. P. Reithmaier, G. Sęk, M. Benyoucef, *Appl. Phys. Lett.* **2021**, *118*, 221101.
[74] C. Nawrath, F. Olbrich, M. Paul, S. L. Portalupi, M. Jetter, P. Michler, *Appl. Phys. Lett.* **2019**, *115*, 023103.
[75] T. Smołka, K. Posmyk, M. Wasiluk, P. Wyborski, M. Gawełczyk, P. Mrowiński, M. Mikulicz, A. Zielińska, J. P. Reithmaier, A. Musiał, M. Benyoucef, *Materials* **2021**, *14*, 21.
[76] K. Takemoto, M. Takatsu, S. Hirose, N. Yokoyama, Y. Sakuma, T. Usuki, T. Miyazawa, Y. Arakawa, *J. Appl. Phys.* **2007**, *101*, 081720.

© 2025 The Author(s). Advanced Quantum Technologies published by Wiley-VCH GmbH

25119044, 0, Downloaded from https://advanced.onlinelibrary.wiley.com/doi/10.1002/qute.202500159 by POLITECNICO DI MILANO, Wiley Online Library on [26/06/2025]. See the Terms and Conditions (https://onlinelibrary.wiley.com/terms-and-conditions) on Wiley Online Library for rules of use; OA articles are governed by the applicable Creative Commons License

[77] S. Kolatschek, C. Nawrath, S. Bauer, J. Huang, J. Fischer, R. Sittig, M. Jetter, S. L. Portalupi, P. Michler, *Nano Lett.* **2021**, *21*, 7740.
[78] S.-W. Xu, Y.-M. Wei, R.-B. Su, X.-S. Li, P.-N. Huang, S.-F. Liu, X.-Y. Huang, Y. Yu, J. Liu, X.-H. Wang, *Photon. Res.* **2022**, *10*, B1.
[79] Z. Ge, T. Chung, Y.-M. He, M. Benyoucef, Y. Huo, *Nano Lett.* **2024**, *24*, 1746.
[80] A. Barbiero, G. Shooter, T. Müller, J. Skiba-Szymanska, R. M. Stevenson, L. E. Goff, D. A. Ritchie, A. J. Shields, *Nano Lett.* **2024**, *24*, 2839.
[81] N. Srocka, A. Musiał, P.-I. Schneider, P. Mrowiński, P. Holewa, S. Burger, D. Quandt, A. Strittmatter, S. Rodt, S. Reitzenstein, G. Sęk, *AIP Adv.* **2018**, *8*, 085205.
[82] N. Srocka, P. Mrowiński, J. Große, M. von Helversen, T. Heindel, S. Rodt, S. Reitzenstein, *Appl. Phys. Lett.* **2020**, *116*, 231104.
[83] M. Jaworski, P. Mrowiński, M. G. Mikulicz, P. Holewa, L. Zeidler, M. Syperek, E. Semenova, G. Sęk, *Opt. Express* **2024**, *32*, 41089.
[84] M. Sartison, L. Engel, S. Kolatschek, F. Olbrich, C. Nawrath, S. Hepp, M. Jetter, P. Michler, S. L. Portalupi, *Appl. Phys. Lett.* **2018**, *113*, 032103.
[85] J. Yang, C. Nawrath, R. Keil, R. Joos, X. Zhang, B. Höfer, Y. Chen, M. Zopf, M. Jetter, S. L. Portalupi, F. Ding, P. Michler, O. G. Schmidt, *Opt. Express* **2020**, *28*, 19457.
[86] J.-H. Kim, T. Cai, C. J. K. Richardson, R. P. Leavitt, E. Waks, *Optica* **2016**, *3*, 577.
[87] C.-M. Lee, M. A. Buyukkaya, S. Harper, S. Aghaeimeibodi, C. J. K. Richardson, E. Waks, *Nano Lett.* **2021**, *21*, 323.
[88] J. Maisch, J. Grammel, N. Tran, M. Jetter, S. L. Portalupi, D. Hunger, P. Michler, *Phys. Rev. B* **2024**, *110*, 165301.
[89] S. Unsleber, Y.-M. He, S. Gerhardt, S. Maier, C.-Y. Lu, J.-W. Pan, N. Gregersen, M. Kamp, C. Schneider, S. Höfling, *Opt. Express* **2016**, *24*, 8539.
[90] J. Liu, R. Su, Y. Wei, B. Yao, S. F. C. d. Silva, Y. Yu, J. Iles-Smith, K. Srinivasan, A. Rastelli, J. Li, X. Wang, *Nat. Nanotechnol.* **2019**, *14*, 586.
[91] S. Liu, K. Srinivasan, J. Liu, *Laser & Photonics Reviews* **2021**, *15*, 2100223.
[92] S. Li, Y. Yang, J. Schall, M. von Helversen, C. Palekar, H. Liu, L. Roche, S. Rodt, H. Ni, Y. Zhang, Z. Niu, S. Reitzenstein, *ACS Photonics* **2023**, *10*, 2846.
[93] A. A. Madigawa, J. N. Donges, B. Gaál, S. Li, M. A. Jacobsen, H. Liu, D. Dai, X. Su, X. Shang, H. Ni, J. Schall, S. Rodt, Z. Niu, N. Gregersen, S. Reitzenstein, B. Munkhbat, *ACS Photonics* **2024**, *11*, 1012.
[94] N. Somaschi, V. Giesz, L. De Santis, J. C. Loredo, M. P. Almeida, G. Hornecker, S. L. Portalupi, T. Grange, C. Antón, J. Demory, C. Gómez, I. Sagnes, N. D. Lanzillotti-Kimura, A. Lemaítre, A. Auffeves, A. G. White, L. Lanco, P. Senellart, *Nat. Photonics* **2016**, *10*, 340.
[95] A. V. Kuhlmann, J. Houel, A. Ludwig, L. Greuter, D. Reuter, A. D. Wieck, M. Poggio, R. J. Warburton, *Nat. Phys.* **2013**, *9*, 570.
[96] D. A. Vajner, P. Holewa, E. Zięba-Ostój, M. Wasiluk, M. von Helversen, A. Sakanas, A. Huck, K. Yvind, N. Gregersen, A. Musiał, M. Syperek, E. Semenova, T. Heindel, *ACS Photonics* **2024**, *11*, 339.
[97] T. Strobel, J. H. Weber, M. Schmidt, L. Wagner, L. Engel, M. Jetter, A. D. Wieck, S. L. Portalupi, A. Ludwig, P. Michler, *Nano Lett.* **2023**, *23*, 6574.
[98] T. Miyazawa, K. Takemoto, Y. Nambu, S. Miki, T. Yamashita, H. Terai, M. Fujiwara, M. Sasaki, Y. Sakuma, M. Takatsu, T. Yamamoto, Y. Arakawa, *Appl. Phys. Lett.* **2016**, *109*, 132106.
[99] R. Joos, S. Bauer, C. Rupp, S. Kolatschek, W. Fischer, C. Nawrath, P. Vijayan, R. Sittig, M. Jetter, S. L. Portalupi, P. Michler, *Nano Lett.* **2024**, *24*, 8626.
[100] L. Wells, T. Müller, R. Stevenson, J. Skiba-Szymanska, D. Ritchie, A. Shields, *Nat. Comm.* **2023**, *14*, 1.
[101] M. Reindl, J. H. Weber, D. Huber, C. Schimpf, S. F. Covre da Silva, S. L. Portalupi, R. Trotta, P. Michler, A. Rastelli, *Phys. Rev. B* **2019**, *100*, 155420.
[102] A. J. SpringThorpe, S. J. Ingrey, B. Emmerstorfer, P. Mandeville, W. T. Moore, *Appl. Phys. Lett.* **1987**, *50*, 77.
[103] U. M. Gür, S. Arslanagić, M. Mattes, N. Gregersen, *Phys. Rev. E* **2021**, *103*, 033301.
[104] A. V. Lavrinenko, J. Lægsgaard, N. Gregersen, F. Schmidt, T. Søndergaard, *Numerical Methods in Photonics*, CRC Press, **2015**.

© 2025 The Author(s). Advanced Quantum Technologies published by Wiley-VCH GmbH

25119044, 0, Downloaded from https://advanced.onlinelibrary.wiley.com/doi/10.1002/qute.202500159 by POLITECNICO DI MILANO, Wiley Online Library on [26/06/2025]. See the Terms and Conditions (https://onlinelibrary.wiley.com/terms-and-conditions) on Wiley Online Library for rules of use; OA articles are governed by the applicable Creative Commons License